J|A|C|S ARTICLES

Published on Web 06/15/2009

One-Step Synthesis of Core−Shell $(Ce_{0.7}Zr_{0.3}O_2)_x(Al_2O_3)_{1-x}$ $[(Ce_{0.7}Zr_{0.3}O_2)@Al_2O_3]$ Nanopowders via Liquid-Feed Flame Spray Pyrolysis (LF-FSP)

Min Kim and Richard M. Laine*

Department of Materials Science and Engineering, University of Michigan, Ann Arbor, Michigan 48109-2136

Received March 7, 2009; E-mail: talsdad@umich.edu

Abstract: We report here the synthesis of $Ce_xZr_{1-x}O_2$ and $(Ce_{0.7}Zr_{0.3}O_2)_x(Al_2O_3)_{1-x}$ core−shell nanopowders in a single step by liquid-feed flame spray pyrolysis (LF-FSP) of the metalloorganic precursors, $Ce(O_2CCH_2CH_3)_3(OH)$, alumatrane $[N(CH_2CH_2O)_3Al]$, and $Zr(O_2CCH_2CH_3)_2(OH)_2$. Solutions of all three precursors in ethanol with ceramic yields of 2.5 wt% were aerosolized with O_2, combusted at temperatures above 1500 °C, and rapidly quenched at ∼1000 °C/ms to form $Ce_xZr_{1-x}O_2$ and $(Ce_{0.7}Zr_{0.3}O_2)_x(Al_2O_3)_{1-x}$ nanopowders of selected compositions, at rates of 50−100 g/h. The resulting, as-processed, materials are unaggregated nanopowders with average particle sizes (APSs) < 20 nm and corresponding specific surface areas of 30−50 m^2/g. The as-processed powders were characterized in terms of phase, particle size, specific surface area, compositions, and morphology by XRD, BET, DLS, SEM, TEM, XPS, TGA-DTA, and FT-IR. LF-FSP provides access to binary $Ce_xZr_{1-x}O_2$ nanopowders and ternary $(Ce_{0.7}Zr_{0.3}O_2)_x(Al_2O_3)_{1-x}$ nanopowders in one step. The obtained $Ce_{0.7}Zr_{0.3}O_2$ powders are solid solutions with a cubic phase. In contrast, LF-FSP of mixtures of the three precursors at specific compositions [x = 0.5, 0.7 for $(Ce_{0.7}Zr_{0.3}O_2)_x@(Al_2O_3)_{1-x}$] provide core−shell nanopowders in a single step. The most reasonable explanation is that there are differences in the rates of condensation, nucleation and miscibility between the gas phase ions that form the $Ce_xZr_{1-x}O_2$ solid solutions and those that condense to δ-Al_2O_3 during processing. These as-produced materials are without microporosity at surface areas of ≥30 m^2/g. Evidence is presented suggesting the formation of $(Ce/Zr)^{3+}$ species in the as-processed $(Ce_{0.7}Zr_{0.3}O_2)_x(Al_2O_3)_{1-x}$ core−shell materials. An accompanying paper indicates that these materials offer significant and novel catalytic activities for hydrocarbon oxidation and deNO_x processes without using platinum as a co-catalyst.

Introduction

The past two decades have witnessed an explosion in efforts directed toward the synthesis, characterization and application of nanoparticles in very diverse fields. Indeed, there are now fields within fields in the study of nanoparticles with major areas of study concerned with metal, metal oxide, metal chalcogen, and metal pnictogen particles among others, and of course studies at the interface between these materials centered for example around core−shell systems.[1−7]

Although the synthesis and characterization of metal and metal oxide nanopowders have received tremendous recent attention, early work on nanoparticles was first conducted in the late 50s and early 60s by researchers exploring methods of making single quantum magnetic particles and related materials for recording media, catalysts and pigments as partially reviewed by Luborsky.[1,3,4]

If we limit discussion to the synthesis of nanoparticles rather than nanorods, whiskers, or nanotubes, there are still numerous preparative approaches described in the literature.[1−10] Although a majority of this research focuses on solution syntheses via direct reactions in high-boiling solvents[5−8] or sol−gel approaches;[12−14] commercial scale synthesis of ultrafine and nanopowders is mostly via gas phase reaction chemistry.[15,16] Thus, many thousands of tons of titania, silica, alumina, and zirconia powders are produced annually primarily by reaction of the volatile metal chlorides in a hydrogen/oxygen flame, reaction 1, in a process called flame spray pyrolysis, FSP. Depending on the conditions the resulting products are either ultrafine <500 nm average particle sizes (APSs) or nanosized <100 nm.

$$MCl_x + H_2 + O_2 \xrightarrow{1200°C} MO_y + HCl + Cl_2 + H_2O, \text{ etc.} \quad (1)$$

Unfortunately, the number of potential ultrafine and nanopowder oxides that can be synthesized by FSP is limited by the number of volatile metal chlorides. Another problem noted in

(1) Reviews: (a) Luborsky, F. E. *J. Appl. Phys.* **1961**, *32*, S171. (b) Cushing, B. L.; Kolesnichenko, V. L.; O'Connor, C. J. *Chem. Rev.* **2004**, *104*, 3893. (c) Swihart, M. T. *Curr. Opin. Colloid Interface Sci.* **2003**, *8*, 127–133. (d) Kruis, F. E.; Fissan, H.; Peled, A. **2004**, *29*, 511. (e) Strobel, R; Pratsinis, S. E. *J. Mater. Chem.* **2007**, *17*, 4743.

(2) Klabunde, K. J. *Free Atoms, Clusters, and Nanoscale Particles*; Academic Press: New York, 1994.

(3) (a) Fabian, R. W.; Sienczyk, J. L.; U.S. Patent 2,884,319. April 1959. (b) Thomas, R.; U.S. Patent 3,281,344. Oct. 1966. (c) Smith, T. W.; U.S. Patent 4,252,671. Feb. 1981.

(4) (a) Dan, N.; Zubris, M.; Tannenbaum, R. *Macromolecules* **2005**, *38*, 9243–9250. (b) Tannenbaum, R.; Zubris, M.; Goldberg, E. P.; Reich, S.; Dan, N. *Macromolecules* **2005**, *38*, 4254.

10.1021/ja9017545 CCC: $40.75

the literature[17,18] has been the great difficulty in using FSP to synthesize mixed-metal oxide powders. This problem arises because of the disparate rates of hydrolysis/oxidation of the individual chlorides even when the resulting mixed-metal oxides are expected to be completely miscible, e.g., SiO_2 and Al_2O_3 readily form aluminosilicates.

In the past decade, we and others have resolved this problem through the development of liquid-feed flame spray pyrolysis (LF-FSP) wherein alcohol solutions of organometallic and preferably metalloorganic precursors (e.g., carboxylates, β-diketonates, and alkoxides) are aerosolized with oxygen and ignited. The combustion process generates flames of 1500−2000 °C and if the combustion derived metal oxide ions are quenched rapidly enough, ∼1000 °C/ms, it is possible to produce a wide variety of unaggregated (therefore easily dispersed) nanopowders whose compositions are determined almost completely by the compositions of the precursors in solution.[17−26] Furthermore, it is possible to produce 100 g/h quantities of mixed-metal oxide nanopowders in the laboratory with APSs <100 nm and frequently <20−30 nm, which equates to specific surface areas (SSAs) of up to 100 m^2/g without internal porosity. Alternately, it is possible to produce up to five different samples/day at 20−30 g quantities.[23−26]

It is important to note at the outset that there are multiple solution chemistry routes to core−shell metal oxide nanopowders;[8,10,11,27,28] however, these routes often lead to amorphous materials that must be heated to crystallize one or both components. Furthermore, this heating typically causes particle aggregation limiting their utility for further processing. In contrast, LF-FSP provides access to fully crystalline core−shell and easily processed nanomaterials. It also offers access to unusual kinetic phases and in some instances by repassing the nanopowders through the LF-FSP system, it provides access to nanopowders of thermodynamically stable phases that are difficult to obtain by traditional processing techniques.[15,16,24−26]

In this paper, we describe efforts to develop routes to binary $Ce_xZr_{1-x}O_2$ solid solution and ternary $(Ce_{0.7}Zr_{0.3}O_2)_x@(Al_2O_3)_{1-x}$ core−shell nanostructured nanoparticles targeting the development of novel catalyst systems for emission control of hydrocarbons and NO_x. In an accompanying paper, we describe high throughput, combinatorial testing of sets of these nanopowders to assess their catalytic activity for promoting oxidation of propane and coincident reduction of NO_x. In the accompanying paper, we find that the LF-FSP produced $Ce_xZr_{1-x}O_2$ and $(Ce_{0.7}Zr_{0.3}O_2)_x(Al_2O_3)_{1-x}$ core−shell nanopowders offer catalytic activities for deNO_x reactions approaching those of Pt containing catalysts but without the need for Pt. Here we present evidence for the possible formation of zirconia suboxide species, ZrO_{2-x}, which may be responsible for this catalytic behavior.

Experimental Section

Materials. Cerium carbonate $[Ce_2(CO_3)_3 \cdot x(H_20)$, 99%] and zirconium carbonate $[2ZrO_2(CO_2) \cdot x(H_2O)$, 99%] were purchased from PIDC Inc. (Ann Arbor, MI). EtOH (99%) was purchased from standard sources and used as received. Alumatrane $[N(CH_2CH_2O)_3Al]$ was prepared as described elsewhere.[25a] Propionic acid ($C_2H_5CO_2H$, 99%) was purchased from Aldrich and used as received.

Precursor Preparation. Precursors with ceramic compositions $[(CeO_2)_{0.7}(ZrO_2)_{0.3}]_x(Al_2O_3)_{1-x}$ ($x = 0.9$, 0.7, 0.5, 0.3, and 0.1) were prepared from mixtures of the following metalloorganics.

Al_2O_3 Precursor. In all cases, alumatrane $[N(CH_2CH_2O)_3Al]$ was used as the Al_2O_3 source. An alumatrane/EtOH solution was prepared containing 10.8 wt % Al_2O_3 per TGA.

Cerium Propionate Precursor: $Ce(O_2CCH_2CH_3)_3(OH)$. Cerium carbonate $[Ce_2(CO_3)_3 \cdot x(H_2O)$, 99%, 70 g, 0.15 mol] was reacted with excess propionic acid (400 mL, 5.44 mol) in a 1 L flask equipped with a still head and an addition funnel. N_2 was

(5) (a) Figlarz, M.; Fiévet, F.; Lagier, J. P. U.S. Patent 4,539,041, Sept. 31985. (b) Fiévet, F.; Lagier, J. P.; Blin, B.; Beaudoin, B.; Figlarz, M. *Solid State Ionics,* **1989**, *32/33*, 198. (c) Kurihara, L. K.; Chow, G. M.; Schoen, P. E. *Nanostruct. Mater.* **1995**, *6*, 607. (e) Laine, R. M.; Sellinger, A.; U.S. Patent 6,551,960. April 22, 2003.

(6) (a) Suh, W. H.; Suslick, K. S. *J. Am. Chem. Soc.* **2005**, *127*, 12007. (b) Skrabalak, S. E.; Suslick, K. S *J. Am. Chem. Soc.* **2005**, *127*, 9990. (c) Suh, W. H. *J. Am. Chem. Soc.* **2005**, *127*, 12007.

(7) (a) Puntes, V. F.; Zanchet, D.; Erdonmez, C. K.; Alivisatos, A. P. *J. Am. Chem. Soc.* **2002**, *124*, 12874. (b) Liu, H.; Guo, J.-H.; Yin, Y.; Augustsson, A.; Dong, C.; Nordgren, J.; Chang, C.; Alivisatos, P.; Thornton, G.; Ogletree, D. F.; Requejo, F. G.; de Groot, F.; Salmeron, M. *Nano Lett.* **2007**, *7*, 1919.

(8) (a) Tsay, J. M.; Pflughoefft, M.; Bentolila, L. A.; Weiss, S. *J. Am. Chem. Soc.* **2004**, *126*, 1926. (b) Kim, S.; Fisher, B.; Eisler, H.-J.; Bawendi, M. *J. Am. Chem. Soc.* **2003**, *125*, 11466.

(9) (a) Grass, R. N.; Athanassiou, E. K.; Stark, W. J. *Angew. Chem.* **2007**, *46*, 4909. (b) Athanassiou, E. K.; Grass, R. N.; Osterwalder, N.; Stark, W. J. *Chem. Mater.* **2007**, *19*, 4847. (c) Ponce, A. A.; Klabunde, K. J. *J. Molec. Catal. A* **2005**, *225*, 1.

(10) Nyutu, E. K.; Conner, W. C.; Auerbach, S. M.; Chen, C.-H.; Suib, S. L. *J. Phys. Chem. C.* **2008**, *112*, 1407.

(11) Chen, T-Y.; Somasundaran, P. *J. Am. Ceram. Soc.* **1998**, *81*, 140.

(12) (a) Chen, Q.; Boothroyd, C.; Tan, G. H.; Sutanto, N.; Soutar, A. M.; Zeng, Z. T. *Langmuir* **2008**, *24*, 650. (b) Yeshchenko, O. A.; Dmitruk, I. M.; Alexeenko, A. A.; Dmytruk, A. A. *J. Phys. Chem. Sol.* **2008**, *69*, 1615.

(13) Masala, O.; Seshadri, R. *J. Am. Chem. Soc.* **2005**, *127*, 9354.

(14) Aslan, K.; Wu, M.; Lakowicz, J. R.; Geddes, C. D. *J. Am. Chem. Soc.* **2007**, *129*, 1524–1525.

(15) Kodas, T. T.; Hampden-Smith, M. J. *Aerosol Processing of Materials*; Wiley-VCH: New York, 1999.

(16) Winterer, M. *Nanocrystalline Ceramics, Synthesis and Structure*; Springer: New York, 2002.

(17) Ulrich, G. D. *Chem. Eng. News* **1984**, *62*, 22.

(18) Gurav, A.; Kodas, T.; Pluym, T.; Xiong, Y. *Aerosol Sci. Technol.* **1993**, *19*, 411.

(19) Burgos-Montes, O.; Moreno, R.; Colomer, M. T.; Fariñas, J. C. *J. Am. Ceram. Soc.* **2006**, *89*, 484.

(20) McCormick, J. R.; Zhao, B.; Rykov, S. A.; Wang, H.; Chen, J. G. *J. Phys. Chem. B.* **2004**, *108*, 17398.

(21) (a) Strobel, R.; Metz, H. J.; Pratsinis, S. E. *Chem. Mater.* **2008**, *20*, 6346. (b) Teoh, W. Y.; Setiawan, R.; Mädler, L.; Grunwaldt, J.-D.; Amal, R.; Pratsinis, S. E. *Chem. Mater.* **2008**, *20*, 4069.

(22) Li, D.; Teoh, W. Y.; Selomulya, C.; Woodward, R. C.; Amal, R.; Rosche, B. *Chem. Mater.* **2006**, *18*, 6403.

(23) Laine, R. M.; Waldner, K.; Bickmore, C.; Treadwell, D. R. U.S. Patent 5,958,361, September 28, 1999.

(24) (a) Kim, M.; Laine, R. M. *J. Cer. Proc. Res.* **2007**, *8*, 129. (b) Kim, M.; Hinklin, T. R.; Laine, R. M. *Chem. Mater.* **2008**, *20*, 5154. (c) Kim, M., Laine, R. M. submitted to *J. Am. Ceram. Soc.*

(25) (a) Hinklin, T.; Toury, B.; Gervais, C.; Babonneau, F.; Gislason, J. J.; Morton, R. W.; Laine, R. M. *Chem. Mater.* **2004**, *16*, 21. (b) Kim, M.; Hinklin, T. R.; Laine, R. M. *Chem. Mater.* **2008**, *20*, 5154. (c) Marchal, J.; Johns, T.; Baranwal, R.; Hinklin, T.; Laine, R. M. *Chem. Mater.* **2004**, *16*, 822. (d) Kim, S.; Gislason, J. J.; Morton, R. W.; Pan, X. Q.; Sun, H. P.; Laine, R. M. *Chem. Mater.* **2004**, *16*, 2336. (e) Azurdia, J. A.; Marchal, J.; Laine, R. M. *J. Am. Ceram. Soc.* **2006**, *89*, 2749. (f) Azurdia, J. A.; Marchal, J.; Shea, P.; Sun, H.; Pan, X. Q.; Laine, R. M. *Chem. Mater.* **2006**, *18*, 731.

(26) (a) Laine, R. M.; Marchal, J. C.; Sun, H. P.; Pan, X. Q. *Nat. Mater.* **2006**, *5*, 710. (b) Laine, R. M.; Marchal, J.; Sun, H. J.; Pan, X. Q. *Adv. Mater.* **2005**, *17*, 830. (c) Hinklin, T. R.; Rand, S. C.; Laine, R. M. *Adv. Mater.* **2008**, *20*, 1270.

(27) (a) Sakai, H.; Kanda, T.; Shibata, H.; Ohkubo, T.; Abe, M. *J. Am. Chem. Soc.* **2006**, *128*, 4944. (b) Xu, Z.; Hou, Y.; Sun, S. *J. Am. Chem. Soc.* **2007**, *129*, 8698. (c) Aslan, K.; Wu, M.; Lakowicz, J. R.; Geddes, C. D. *J. Am. Chem. Soc.* **2007**, *129*, 1524. (d) Xu, Z.; Hou, Y.; Sun, S. *J. Am. Chem. Soc.* **2007**, *129*, 8698.

(28) (a) Teng, X.; Yang, H. *J. Am. Chem. Soc.* **2003**, *125*, 14559. (b) Lai, J.; Shafi, K. V. P. M.; Ulman, A.; Loos, K.; Popovitz-Biro, R.; Lee, Y.; Vogt, T.; Estournes, C. *J. Am. Chem. Soc.* **2005**, *127*, 5730. (c) Deng, Y.; Qi, D.; Deng, C.; Zhang, X.; Zhao, D. *J. Am. Chem. Soc.* **2008**, *130*, 28.

sparged directly through the solution (2 psi pressure) as the solution was heated at 120 °C/2 h to distill off ~150 mL of liquid (water and propionic acid). The ceramic loading of the resulting precursor was 9 wt % as determined by TGA. We describe the isolation and characterization of this precursor elsewhere.[24b]

Zirconium Propionate Precursor: $Zr(O_2CCH_2CH_3)_2(OH)_2$. Zirconium carbonate [$ZrO_2(CO_2)\cdot x(H_2O)$, 99%, 150 g, 0.34 mol] was reacted with excess propionic acid (500 mL, 6.80 mol) in a 1 L flask equipped with a still head and an addition funnel. N_2 was sparged directly through the solution (2 psi pressure) as the solution was heated at 120 °C/2 h with magnetic stirring to distill off ~150 mL of liquid (water and propionic acid). The ceramic loading of the resulting precursor was 11 wt % as determined by TGA. We describe the isolation and characterization of this precursor elsewhere.[22]

Analytical Studies. Information concerning the experimental procedures used for the following analytical tools are provided in the experimental section in the Supporting Information including X-ray powder diffraction (XRD), dynamic laser light scattering (DLS), thermal gravimetric and differential thermal analysis (TGA/DTA), specific surface area (SSA, BET) analyses, scanning electron microscopy (SEM), transmission electron microscopy (SEM), FTIR spectral analyses, and X-ray photoelectron spectroscopy (XPS).

Liquid Feed-Flame Spray Pyrolysis (LF-FSP). The apparatus used for LF-FSP is comprised of an aerosol generator, a combustion chamber, and an electrostatic powder collection system described elsewhere.[24−26] The precursor solution was pumped through the aerosol generator at a rate controlled by the ceramic yield of the solution. Typically, more concentrated (5 wt % ceramic yield) solutions were pumped at 100 mL/min to avoid producing large particles (200−1000 nm).[24−26] Solutions with lower ceramic yields were pumped at 400 mL/min. Here we used precursor solutions with 2.5 wt % ceramic yield for each batch at the pumping rate of 300 mL/min. The solution was atomized with oxygen to form an aerosol and ignited by two methane/oxygen pilot torches, while the pressure was kept at 20 psi. Combustion produces temperatures >1500 °C[24−26] and nanosized oxide powders are collected in electrostatic precipitators (ESP).

Results and Discussion

The LF-FSP process, described in detail elsewhere,[24−26] aerosolizes solutions of single and mixed-metal alkoxides and/or carboxylates dissolved in alcohol (typically EtOH) using oxygen. The aerosol is ignited in a quartz combustion chamber generating flame temperatures of 1500−2000 °C depending on the processing conditions, the precursor, and the alcohol used. The temperature drops rapidly to less than 400 °C in ~1.5 m leading to very rapid quenching of the gas entrained ceramic "soot." This soot is then collected in electrostatic precipitators downstream from the combustion chamber and consists of unaggregated nanopowders of the exact composition found in the original solution. Typical production rates are 50−100 g/h depending on the precursor. The resulting APSs are 10−150 nm depending on processing conditions giving SSAs of 20−100 m^2/g. They are most frequently single crystal particles that disperse readily in common solvents.

We have used LF-FSP to produce a wide variety of single and binary-metal oxide nanopowders[24−26] along the $(MO_z)_x(Al_2O_3)_{1-x}$ tielines were M = Ni, Ti, Co, Mg, Y, Cu, Zr, and Ce. The as-produced binary nanopowders are also unaggregated with SSAs of 30−60 m^2/g and APSs of 15−30 nm. However, we recently discovered that under some conditions, it is possible to make crystalline core−shell nanoparticles with novel properties the subject of this and recent papers.[24] To frame the current work properly, it is pertinent to provide a brief background.

Initial studies on LF-FSP benchmarked the process against FSP for production of nano-Al_2O_3.[25a,b] Both methods produce similar high surface area, micropore free δ- rather than α-Al_2O_3 nanopowders despite flame temperatures exceeding the normal phase transformation temperature near 1200 °C.[25] The possible reasons for this are addressed elsewhere.[26a] These same studies demonstrated that any impurities in the starting precursor are incorporated into the resulting δ-Al_2O_3 nanopowders.[23−26,29]

The potential to purposely introduce impurities (dopants) combined with the fact that the density of δ-Al_2O_3 is 3.5 g/cm^3 (vs 3.99 g/cm^3 for α-Al_2O_3) indicating a more open crystal lattice suggested efforts to incorporate large dopant ions, especially rare earths (REs). The motivation for this work was two-fold. One was to use LF-FSP to replace Al^{3+} with RE^{3+} ions to develop novel phosphors. The second was to inhibit the transformation temperature of δ- to α-Al_2O_3 to stabilize it as a potential catalyst support given that REs are known to inhibit both phase transformations and grain growth in alumina.[30,31] An important aspect of this work was the fact that most dopant studies coat alumina particles with RE dopants whereas LF-FSP offers the opportunity to place the dopant directly in the lattice perhaps greatly affecting (slowing) transformation rates.

Efforts to incorporate REs into the δ-Al_2O_3 lattice were quite successful as LF-FSP provides nanopowders that retain the δ-Al_2O_3 crystal structure yet contain up to 5 wt % Ce^{3+} ions before generating Ce-magnetoplumbite ($CeAl_{11}O_{18}$).[24b] Thus, LF-FSP provides access to a δ-Al_2O_3 wherein a significant fraction of M^{3+} lattice sites normally occupied by Al^{3+} are instead occupied by Ce^{3+}. These results were extended to a wide variety of RE^{3+} ions.[32] *In contrast, the solubility of RE^{3+} in α-Al_2O_3 is limited to ~10 ppm.*[31]

Surprisingly, not only did these new nanopowders act as phosphors,[32] they also offered unique properties acting as "laser paints" and exhibiting incoherent lasing by trapping light within virtual cavities.[33] In particular, cathodoluminscence experiments using Ce^{3+} doped δ-Al_2O_3 nanopowders demonstrate continuous wave UV lasing.[32b] These same Ce^{3+} doped δ-Al_2O_3 nanopowders also offer considerable resistance to sintering coincident with elevated phase transformation temperatures (to α-Al_2O_3).[33]

As noted above, because LF-FSP permits facile processing of multiple samples, efforts were made to extend these studies to their logical conclusion by producing samples along the entire tie-line both for completeness but also to explore opportunities to make novel kinetic materials leading to the discovery of core−shell or nanostructured nanoparticles, CeO_x@δ-Al_2O_3.[24b]

(29) Sutorik, A. C.; Neo, S. S.; Hinklin, T.; Baranwal, R.; Treadwell, D. R.; Narayanan, R.; Laine, R. M. *J. Am. Ceram. Soc.* **1998**, *81*, 1477–1486.
(30) Ragan, D. D.; Mates, T.; Clarke, D. R. *J. Am. Ceram. Soc.* **2003**, *86*, 541–545.
(31) Thompson, A. M.; Soni, K. K.; Chan, H. M.; Harmer, M. P.; Williams, D. B.; Chabala, J. M.; Levi-Setti, R. *J. Am. Ceram. Soc.* **1997**, *80*, 373–376.
(32) (a) Williams, G. R; Bayram, S. B; Rand, S. C; Hinklin, T; Laine, R. M. *Phys. Rev. A.* **2001**, *65*, 013807. (b) Ultraviolet nanophosphors, B.; Li, T; Hinklin, R; Laine, S *J. Lumin.* **2007**, *122−123*, 345−347. (c) Li, C. B; Williams, G; Rand, S. C; Hinklin, T; Laine, R. M. *Opt. Lett.* **2002**, *27*, 394–396. (d) Laine, R. M; Hinklin, T; Williams, G; Rand, S. C. *Mater. Sci. Forum* **2000**, *343−346*, 500−10. (e) Li, D. B; Oliveira, S. L.; Rand, S. C. Azurdia; J, A; Hinklin, T. R; Marchal, J. C.; Laine, R. M. *J. Appl. Phys.* **2007**, *101*, 053534.
(33) Redmond, S. M; Armstrong, G. L; Chan, H.-Y; Mattson, E; Mock, A; Li, B; Potts, J. R; Cui, M; Rand, S. C; Oliveira, S. L; Marchal, J.; Hinklin, T.; Laine, R. M *J. Opt. Soc. Am. B.* **2004**, *21*, 214–222.
(34) Hinklin, T; Ph, D. *Dissertation, University of Michigan* **2006**, 6.

The discovery of core−shell nanoparticles prompted efforts to also examine zirconia analogues but for completely different reasons.

Tetragonal, zirconia (t-ZrO_2) toughened α-Al_2O_3 (ZTA) is one of the more important new, hard and "tough" ceramic materials receiving a great deal of attention especially for prosthetic implants, cutting tools, kitchen knives and even photonic microdevices.[35−38] The normally very high α-Al_2O_3 sintering temperatures required to produce fully dense, optimal ZTA materials can require hot isotatic pressing at temperatures exceeding 1400 °C and pressures of up to 100 MPa to achieve >99.8% densities.

To stabilize the tetragonal phase, which provides the toughening properties, both yttria and ceria dopants are added in up to 3 wt %. We now find it possible to escape the high temperatures, pressures and dopants required to densify ZTA by using LF-FSP to produce a number of t-ZrO_x@δ-Al_2O_3 nanopowders.[24a] These powders allow pressureless sintering to completely dense monoliths at temperatures just above 1100 °C. Basically the δ-Al_2O_3 shell sinters at much lower temperatures even than nano-α-Al_2O_3.[26a] The resulting dense materials have final grain sizes <200 nm, the δ-Al_2O_3 shell transforms to α-Al_2O_3 while the encapsulated t-ZrO_2 particle remains without the need to add a stabilizing agent and the resulting monoliths offer transformation toughening.[26c] Thus, the baseline studies that allow us to understand the work reported here were originally directed toward other objectives than those reported here.

Thus the current study, while building on these previous studies, has completely different objectives. Catalytic control of exhaust emissions from both internal combustion engines and more recently diesel engines has been the subject of an enormous number of studies with multiple, highly cited reviews already written.[39−47] Intense efforts to optimize three-way auto exhaust catalysts, TWCs have occurred over the past 30 years for auto exhaust emission control only. Current TWCs used in more than 10 million new automobiles annually in the U.S. alone, are catalyst systems largely based on high surface area ceria−zirconia solid solutions applied to monolithic honeycomb supports (typically cordierite, $2MgO\cdot 2Al_2O_3\cdot 5SiO_2$) through the use of a "washcoating" method that employs sol−gel derived alumina to affix the $Ce_{1-x}Zr_xO_2$ powders and a precious metal, usually Pd, to the support. The most commonly used TWC $Ce_{1-x}Zr_xO_2$ solid solution is $Ce_{0.7}Zr_{0.3}O_2$. The CeO_x component stores and then delivers oxygen needed to oxidize residual hydrocarbons and CO found in the exhaust whereas the Pd component promotes reduction of NO_x species in the exhaust. Both are thought to also promote the water−gas shift reaction. ZrO_x is added to form a solid solution that is generally considered to prevent CeO_x sintering during operation allowing the TWC to maintain its catalytic activity over extended periods.

The entire process of preparing the washcoat system including the alumina consists of some 10 steps.[39] We realized that it might be possible to use LF-FSP processing to produce the same combination of components in a single step and even coat the honeycomb monolith by placing it directly in the flame. If possible, we would save multiple steps, reducing costs in terms of equipment needed and waste byproducts generated.

This then motivated the current efforts to use LF-FSP to produce high SSA, nonporous $Ce_{1-x}Zr_xO_2/Al_2O_3$ materials in one step as a prelude to exploring their utility for emission treatment catalysts as described in an accompanying paper.[24,48] *Despite the extensive literature on $Ce_{0.7}Zr_{0.3}O_2$ materials,*[39−47] *our findings below and in the accompanying paper point to very novel properties, not seen previously.*

Of particular importance is the fact that the quality of the nanopowders produced depends strongly on the type of precursor used. In our studies on the LF-FSP synthesis of δ-Al_2O_3, we determined that metal nitrates although relatively inexpensive are actually very poor precursors for LF-FSP processing because they tend to form large (200−2000 nm) hollow particles (by a spray pyrolysis mechanism), whereas alumatrane $N(CH_2CH_2O)_3Al$ provides access to powders with SSAs ≈ 60−100 m^2/g.[25] Furthermore, combustion flame temperatures typically have no influence on the quality of the nanopowders produced or the phase.[24−26] It appears that the quenching rate is the primary variable that controls what phases form, the degree of particle aggregation, and to some extent particle sizes.[24−26]

Sutorik and Baliat briefly reported using LF-FSP to make $Ce_{1-x}Zr_xO_2$ solid solutions.[49] More detailed recent studies made by Stark, Jossen et al.[50] also discuss the oxygen storage capacity of $Ce_{0.5}Zr_{0.5}O_2$ nanopowders made using laminar flow LF-FSP.[50] The current work goes one step further than these previous studies in that it explores the coincident introduction of an immiscible alumina component in an attempt, as noted above, to develop a single-step "washcoat" process. Thus, we illustrate an approach to the one step production of $Ce_xZr_{1-x}O_2$ solid solutions coated with imperfect δ-Al_2O_3 shells with essentially any composition desired. The imperfect shells are necessary to obtain good catalytic properties.

For this study, 70:30 Ce/Zr ratios of their propionate precursors were used with varying amounts of an alumatrane precursor (see Experimental Section for details). The total ceramic loadings in EtOH solutions were kept to 2.5 wt % to minimize viscosity problems. These solutions were aerosolized with O_2 and combusted to produce $Ce_{1-x}Zr_xO_2$ and $[(CeO_2)_{0.7}(ZrO_2)_{0.3}]_x@(Al_2O_3)_{1-x}$ ($x = 0.1-0.9$) composition nanopowders at rates of 50−100 g/h. The resulting materials are unaggregated nanopowders with SSAs of 45 ± 5 m^2/g without microporosity.

In the following sections we begin by discussing the Al_2O_3, CeO_2, and ZrO_2 LF-FSP precursors. A discussion of LF-FSP processing follows and thereafter we describe the detailed

(35) Piconi, C.; Maccauro, G. *Biomaterials* **1999**, *20*, 1–25.
(36) Ighodaro, O. L.; Okoli, O. I. *Int. J. Appl. Ceram. Technol* **2008**, *5*, 313–323.
(37) Li, X. S.; Low, I. M. *J. Mater. Sci. Lett.* **1993**, *12*, 1916–1919.
(38) Chen, W.; Kirihara, S.; Miyamoto, Y. *Int. J. Appl. Ceram. Technol.* **2008**, *5*, 353–359.
(39) Flytzani-Stephanopoulos, M. *Mater. Res. Soc. Bull.* **2001**, 885–9.
(40) Jen, H. W.; Graham, G. W.; Chun, W.; McCabe, R. W.; Cuif, J. P.; Deutsch, S.; Touret, O. *Cat. Today* **1999**, *50*, 309.
(41) Gélin, P.; Primet, M. *Appl. Catal. B* **2002**, *39*, 1–37.
(42) Kaspar, J.; Fornasiero, P. *J. Solid State Chem.* **2003**, *171*, 19–29.
(43) Ozawa, M. *J. Alloys Cmpds.* **1998**, *275−277*, 886−890.
(44) Sugiura, M. *Catal. Surv. Asia* **2003**, *7*, 77–87.
(45) Shelef, M.; McCabe, R. W. *Catal. Today* **2000**, *62*, 35.
(46) Ghandi, H. S.; Graham, G. W.; McCabe, R. W. *J. Catal.* **2003**, *216*, 433.
(47) (a) Marecot, P.; Pirault, L.; Mabilon, G.; Prigent, M.; Barbier, J. *Appl. Catal. B* **1994**, *5*, 57. (b) Juan, R. G.; Miguel, A. G.; Jean-Louis, M.; Pilar, G.; Gilbert, B. *Appl. Catal. B* **2000**, *25*, 19.
(48) Weidenhof, B.; Reiser, M.; Stöwe, K.; Maier, W. F.; Kim, M.; Azurdia, J.; Gulari, E.; Sekers, E.; Barks, A.; Laine, R. M. *J. Am. Chem. Soc.* **2009**, *131*, http://dx.doi.org/ja8091345.
(49) Sutorik, A. C.; Baliat, M. S. *Mat. Sci. For.* **2002**, *386*, 371.
(50) (a) Stark, W. J.; Maciejewski, M.; Madler, L.; Pratsinis, S. E.; Baiker, A. *J. Catal.* **2003**, *220*, 35. (b) Jossen, R.; Heine, M. C.; Pratsinis, S. E.; Akhtar, M. K. *Chem. Vapor Dep.* **2006**, *12*, 614–619. (c) Jossen, R.; Heine, M. C.; Pratsinis, S. E; Akhtar, M. K; Jossen, b.; Pratsinis, R.; Stark, S. E.; Madler, W. J *L. J. Am. Ceram. Soc.* **2005**, *88*, 1388.

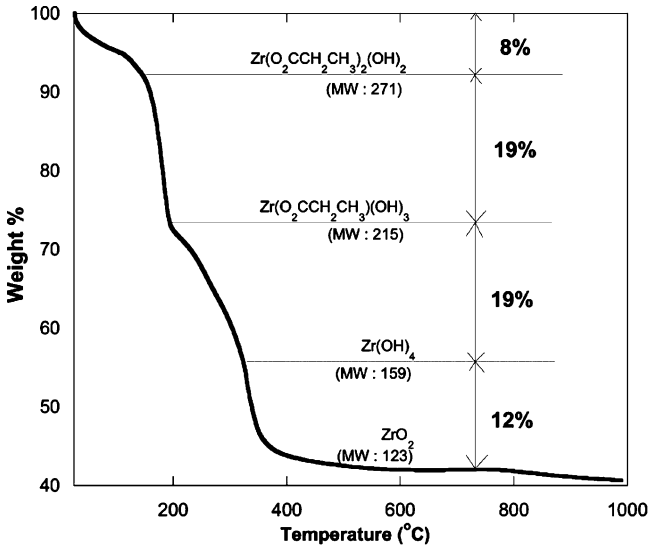

Figure 1. TGA of $Zr(O_2CCH_2CH_3)_2(OH)_2$ ramped at 10 °C/min in synthetic air.[24a]

characterization of the $Ce_{1-x}Zr_xO_2$ and $[(CeO_2)_{0.7}$-$(ZrO_2)_{0.3}]_x@(Al_2O_3)_{1-x}$ ($x = 0.1-0.9$) materials using various analytical tools including XRD, BET, DLS, FTIR, TGA-DTA, SEM, TEM, and XPS.

Precursors and Precursor Formation. We previously reported the characterization of alumatrane $[N(CH_2CH_2O)_3Al]$, cerium propionate $Ce(O_2CCH_2CH_3)_3(OH)$, zirconium propionate $Zr(O_2CCH_2CH_3)_2(OH)_2$, and their use as precursors in LF-FSP for the synthesis of δ-alumina, $(CeO_x)_{1-x}(Al_2O_3)_x$ and $(ZrO_2)_{1-x}(Al_2O_3)_x$ nanopowders.[24,26] These precursors have thermal decomposition patterns similar to other metal carboxylate precursors studied previously.[24−26]

For example, Figure 1 shows a TGA trace for $Zr(O_2CCH_2$-$CH_3)_2(OH)_2$.[24] Initial mass losses (8%) are due to propionic acid of recrystallization. Thereafter, mass loss events are attributed to the decomposition of the propionate ligands as suggested in reactions 1−3.[24−26]

$$Zr(O_2CCH_2CH_3)_2(OH)_2 \rightarrow Zr(O_2CCH_2CH_3)(OH)_3 + CH_3CH{=}C{=}O$$
$$\text{Calcd (Found) Mass Losss} = 19.01\%\ (19\%)$$
$$Zr(O_2CCH_2CH_3)(OH)_3 \rightarrow Zr(OH)_4 + CH_3CH{=}C{=}O$$
$$\text{Calcd (Found) Mass Losss} = 19.01\%\ (19\%) \quad (2)$$

$$Zr(OH)_4 \rightarrow ZrO_2 + 2H_2O$$
$$\text{Calcd (Found) Mass Losss} = 12.22\%\ (12\%) \quad (3)$$

Final ceramic yields (42% for ZrO_2) are within experimental error of the calculated value (41.75%) from the decomposition of the precursor $[Zr(CH_3CH_2COO)_2(OH)_2]$ to ZrO_2 and are as expected on the basis of previous studies.[24−26]

XRD Studies. XRD was used to characterize the phase compositions of as-processed LF-FSP nanopowders. The XRD patterns (Figure S1, Supporting Information) show that the (111) peak of cubic ceria shifts from its standard position 28.55° 2θ to 28.91° 2θ in the $Ce_{0.7}Zr_{0.3}O_2$ composition. We attribute this (111) peak shift to the formation of a solid solution. Because the standard peak position for the ceria (111) peak (PDF file: 43-1002) is 28.55° 2θ, and that for the zirconia (111) peak (PDF file: 42-1164) is 29.80° 2θ, we can calculate the $Ce_{0.7}Zr_{0.3}O_2$ (111) peak position, using Vegard's law, as 28.92° 2θ. This matches the 28.91° 2θ peak position found for our $(CeO_2)_{0.7}$-$(ZrO_2)_{0.3}$ composition within the limits of XRD resolution (±0.02° 2θ).

For the samples Ce/Zr = 1:1 and 3:7, we observe phase separation of the two possible phases (cubic ceria, t-zirconia) from the data analysis (see Experimental Section). This contrasts with the work of Sutorik and Baliat[49] and with Stark, Jossen et al.[50] where at 1:1 and 3:7 only the solid solutions were observed. The SSAs of Sutorik and Baliat were ∼15 m^2/g, suggesting some influence of particle size and/or processing conditions on the product phase. In contrast, the SSAs of Stark et al.[50] were higher than those reported here but were made under laminar rather than turbulent flow conditions and with production rates at 3−4 vs 50−100 g/h here. Thus, this does not seem to be the explanation. Another possible explanation is presented below on the basis of the XPS studies.

The Ce/Zr = 7:3 composition is that often used in commercial three-way auto exhaust catalysts or TWCs[39−47] and is the reason we chose $Ce_{0.7}Zr_{0.3}O_2$ for the work reported here. Thus, only the alumina content was varied in these studies with four separate samples made at 10, 30, 50, or 70 mol % Al_2O_3. Therefore the powder sample XRDs shown in Figure S2 were produced using a propionate precursor system formulated to a $Ce_{0.7}Zr_{0.3}O_2$ composition and then mixed with $[Al(OCH_2CH_2)_3N]$ to obtain ternary compositions $[Ce_{0.7}Zr_{0.3}O_2]_x(Al_2O_3)_{1-x}$ ($x = 0.1-0.9$).

By comparison with the XRD of $Ce_{0.7}Zr_{0.3}O_2$ in Figure S1, we reproducibly generate the same cubic $(CeO_2)_{0.7}(ZrO_2)_{0.3}$ solid solution with alumina. The (111) peak position of the four different $[Ce_{0.7}Zr_{0.3}O_2]_x(Al_2O_3)_{1-x}$ samples in Figure S2 (28.93° 2θ) is close to the calculated (111) peak position of $Ce_{0.7}Zr_{0.3}O_2$ (28.92° 2θ) within the limits of the XRD resolution (±0.02° 2θ).

Samples with higher $Ce_{0.7}Zr_{0.3}O_2$ loadings make it difficult to observe the δ-Al_2O_3 component in XRD patterns due to the relative peak intensity differences from the higher "z" Ce/Zr materials.

Average Particle Sizes (APSs). The APSs for these materials were estimated from Debye−Scherer line broadening, their SSAs (Table 1) and via DLS for the $(CeO_x)_{0.5}@(Al_2O_3)_{0.5}$ and $(Ce_{0.7}Zr_{0.3}O_2)_{0.5}@(Al_2O_3)_{0.5}$ nanopowders. The first two methods give very similar results. APS values for all of the powders generated are 10−15 nm. The average SSAs for the Ce/Zr samples are ∼33 ± 2 m^2/g, and those for the Ce/Zr/Al samples are 45 ± 2 m^2/g. Figure S3 DLS data show APSs of 40−50 and 60−80 nm for $(CeO_x)_{0.5}@(Al_2O_3)_{0.5}$ and $(Ce_{0.7}Zr_{0.3}O_2)_{0.5}@(Al_2O_3)_{0.5}$, respectively.

Note that the higher z value of the Ce/Zr component might be expected to make it difficult to determine particle sizes from X-ray line broadening. Fortunately, the BET derived values are similar. Furthermore, for the higher alumina loaded samples, the alumina might be expected to dominate the observed surface areas and therefore the particle sizes. The fact that the data are uniform for both methods over all types of powders suggests that both measurement methods are valid. However, DLS, SEM, and TEM provide further substantiation.

Although the DLS data (Figure S3) offer particle sizes roughly double those determined by BET and line broadening, the DLS data rely on standards (see Supporting Information, experimental section) to estimate particle sizes none of which are smaller than 300 nm. As such, the precision of the DLS

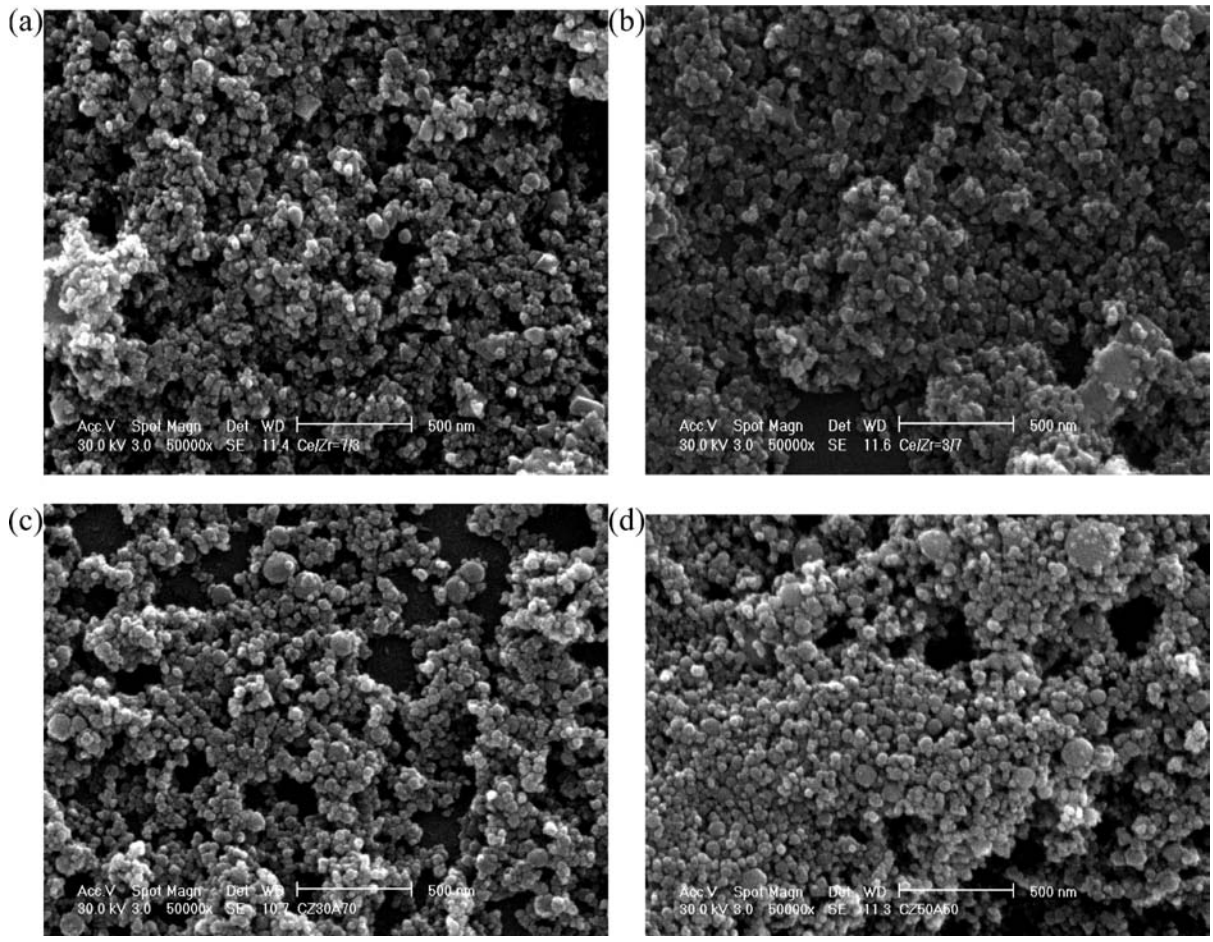

Figure 2. SEM images of (a) $(CeO_2)_{0.7}(ZrO_2)_{0.3}$, (b) $(CeO_2)_{0.3}(ZrO_2)_{0.7}$, (c) $[(CeO_2)_{0.7}(ZrO_2)_{0.3}]_x(Al_2O_3)_{1-x}$ for $x = 0.7$, and (d) $[(CeO_2)_{0.7}(ZrO_2)_{0.3}]_x(Al_2O_3)_{1-x}$ for $x = 0.5$.

Table 1. APSs and SSAs of as-produced LF-FSP Samples

sample	Debye−Scherer particle size (nm)	BET-derived particle size (nm)	SSA (m^2/g)
$[(CeO_2)_{0.7}(ZrO_2)_{0.3}]_x(Al_2O_3)_{1-x}$ for $x = 0.9$	16	20	42
$[(CeO_2)_{0.7}(ZrO_2)_{0.3}]_x(Al_2O_3)_{1-x}$ for $x = 0.7$	13	22	45
$[(CeO_2)_{0.7}(ZrO_2)_{0.3}]_x(Al_2O_3)_{1-x}$ for $x = 0.5$	13	23	46
$[(CeO_2)_{0.7}(ZrO_2)_{0.3}]_x(Al_2O_3)_{1-x}$ for $x = 0.3$	11	24	47
$(CeO_2)_{0.1}(ZrO_2)_{0.9}$	16	28	32
$(CeO_2)_{0.3}(ZrO_2)_{0.7}$	16	28	32
$(CeO_2)_{0.5}(ZrO_2)_{0.5}$	16	28	32
$(CeO_2)_{0.7}(ZrO_2)_{0.3}$	16	26	33
$(CeO_2)_{0.9}(ZrO_2)_{0.1}$	16	22	36

data cannot be confirmed. One might argue that the DLS data suggest the formation of agglomerates or even aggregates; however, then the interpretation would be that these are two or three particle agglomerates or aggregates. Given the small size distribution, this argument seems inappropriate. However, it is important to note that the DLS do not show a bimodal distribution of particle sizes. In addition, the TEM data shown below suggest that the DLS particle size data may be high.

SEM. SEM images (Figures 2) are presented to demonstrate the uniformity of both powder systems. SEM resolution is insufficient to carefully characterize individual particles, but it does provide a view of the general population. The goal here is to demonstrate that the particle populations produced by LF-FSP do not include any obvious micrometer-size particles; although there are some weak agglomerates. Bell and Rodriguez demonstrated that LF-FSP δ-Al_2O_3 nanopowders disperse perfectly without any evidence of aggregates.[51]

Table 2. Possible Maximum Residual $(Ce_{0.7}Zr_{0.3})^{3+}$ Species in δ-Alumina

sample	mass gain as O_2 content (wt %)	possible maximum $(Ce_{0.7}Zr_{0.3})^{3+}$ species (mol ±0.1%)[a]
CZ30A70	0.16	0.3
CZ50A50	0.18	0.3
CZ70A30	0.20	0.4

[a] Assumes all reduced species are $(Ce_{0.7}Zr_{0.3})^{3+}$.

TEM Images. Discussions of actual size/size distributions are not appropriate if based solely on TEM micrographs, unless combined with the XRD, BET, and/or DLS results. To begin with, Figure S4 shows a TEM image of as-shot $Ce_{0.7}Zr_{0.3}O_2$. Faceted crystals are observed, similar to those seen by Stark, Jossen, et al.[50]

Figure 3 TEMs of $(Ce_{0.7}Zr_{0.3}O_2)_{0.5}@(Al_2O_3)_{0.5}$ and $(Ce_{0.7}Zr_{0.3}O_2)_{0.3}@(Al_2O_3)_{0.7}$ particles reveal well-defined lattice fringes indicating formation of single crystal cores. The (111) plane *d*-spacings for both are the same, 3.07 Å, confirming the formation of a cubic $Ce_{0.7}Zr_{0.3}O_2$ solid solution per Figure S2. Moreover, the combined XRDs match those of the individual component XRDs of $Ce_{0.7}Zr_{0.3}O_2$ solid solutions and δ-Al_2O_3.[24a]

(51) Bell, N. S.; Rodriguez, M. A. *J. Nanosci. Nanotechnol.* **2004**, *4*, 283.

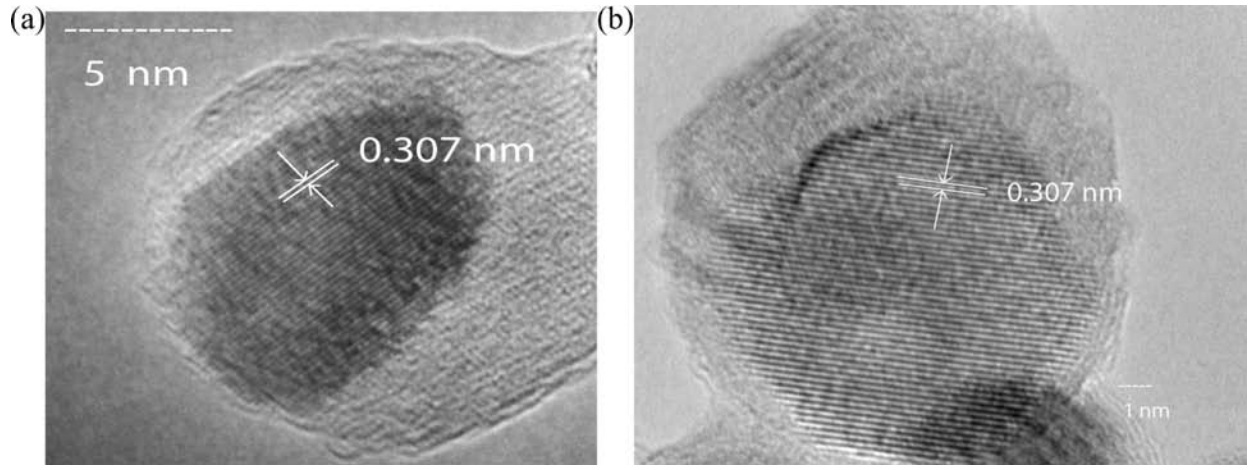

Figure 3. (a) TEM images of $(Ce_{0.7}Zr_{0.3}O_2)_{0.5}(Al_2O_3)_{0.5}$ and (b) $(Ce_{0.7}Zr_{0.3}O_2)_{0.3}(Al_2O_3)_{0.7}$.

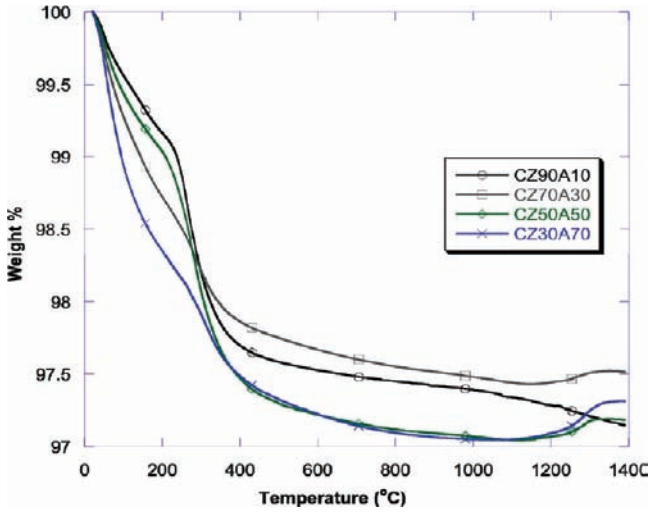

Figure 4. TGA of as-processed $(Ce_{0.7}Zr_{0.3}O_2)_x(Al_2O_3)_{1-x}$ ramped at 10 °C/min/air.

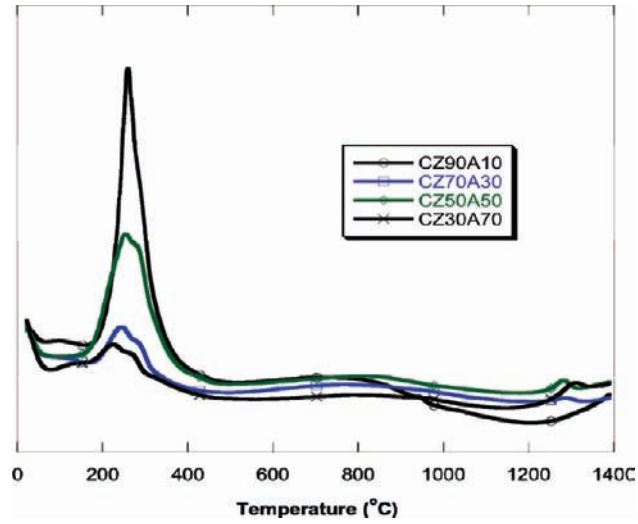

Figure 5. DTA of as-processed $(Ce_{0.7}Zr_{0.3}O_2)_x(Al_2O_3)_{1-x}$ nanopowders.

It is important to note that because the T_m's of both oxides are well above LF-FSP flame temperatures, particle growth must occur by gas phase nucleation followed by gas to solid addition of ions with preferential growth on selected crystal planes. Because Al_2O_3 has a lower vaporization temperature (3000 °C) than CeO_2 (3906 °C) or ZrO_2 (5155 °C),[52,53] ZrO_2 and CeO_2 should co-condense and nucleate first followed by Al_2O_3 in LF-FSP processing. Thus, we initially assumed that $Ce_{0.7}Zr_{0.3}O_2$ solid-solution single crystal nanoparticles form first during quenching, then δ-alumina wets the $Ce_{0.7}Zr_{0.3}O_2$ nanoparticles forming core−shell nanopowders relatively uniformly.

However, the LF-FSP derived $[Ce_{0.7}Zr_{0.3}O_2]_x@(Al_2O_3)_{1-x}$ nanopowders shown in Figure 3, in contrast to pure CeO_2, $Ce_{0.7}Zr_{0.3}O_2$, or $Ce_{0.5}Zr_{0.5}O_2$,[50] are spherical with APSs typically <30 nm with the vast majority <20 nm. Furthermore, the single crystal cores are also spherical. One conclusion discussed in more detail below is that the particle growth mechanisms for the two sets of materials appears to be quite different, *greatly influenced by the presence of AlO_x ions in the gas phase* which may also influence their catalytic behavior.

FTIR Studies. Once particle morphologies were characterized, a detailed picture of particle surface chemistries and thermal behavior was developed through FTIR examination per Figure S5.

All of the materials exhibit weak νO−H absorptions in the 3700−2500 cm^{-1} region, attributable to surface hydroxyls arising from both physi- and chemisorbed water.[54] For the two Al_2O_3-rich samples (CZ5050, CZ30A70), νC−H bands were observed between 3000 and 2700 cm^{-1}, indicating traces of hydrocarbons on the surfaces.[54]

From 1800 to 1400 cm^{-1}, peaks attributable to traces of surface confined CO_2 and carbonates are observed again in accord with those seen for pure δ-Al_2O_3.[25a] Peak intensities for the CO_2 and carbonates are proportional to the amount of Al_2O_3. Absorption bands in the 1000−400 cm^{-1} region correspond to two νAl−O bands at 810 (stretching vibrations of tetrahedrally coordinated Al−O) and 610 cm^{-1} (octahedral coordination).[54,55] The νCe−O band (470 cm^{-1})[56] is not seen clearly because of the limits of the instrument.

TGA−DTA Studies. Figure 4 records the mass loss events for the $(Ce_{0.7}Zr_{0.3}O_2)_x@(Al_2O_3)_{1-x}$ nanopowders. All as-

(52) *CRC Handbook of Chemistry and Physics*, 80th ed.; CRC Press: Boca Raton, FL, 1999.
(53) Peri, J. B. *J. Phys. Chem.* **1965**, *69*, 211.
(54) Tarte, P. *Spectrochim. Acta* **1967**, *23A*, 2127.
(55) Saniger, J. M. *Mater. Lett.* **1995**, *22*, 109.
(56) Harrison, P. G.; Daniell, W. *Chem. Mater.* **2001**, *13*, 1708.

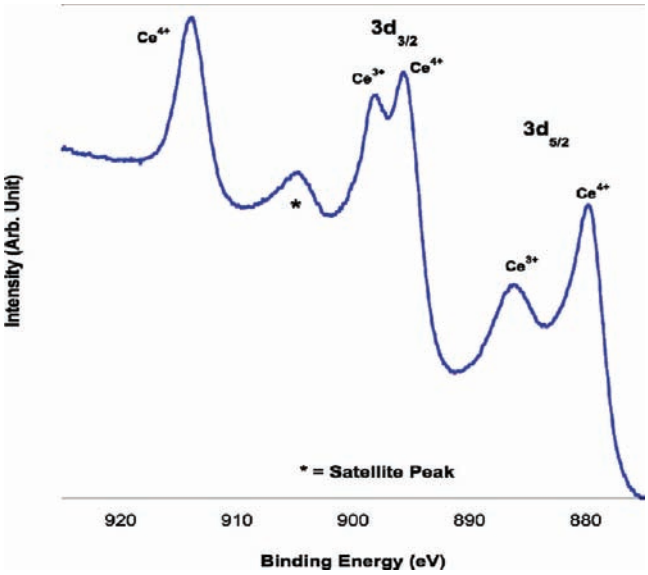

Figure 6. XPS of $Ce^{3+/4+}$ in CZ50A50 sample.

Table 3. Quantification of $(CeO_x)_x(Al_2O_3)_{1-x}$ XPS Data[24]

sample	Ce^{3+}/Ce^{4+} ratio
6 mol % CeO_x in Al_2O_3	0.17
75 mol % CeO_x in Al_2O_3	0.19

processed powders exhibit 1−1.5 wt % mass loss up to ~300 °C, attributed to evolution of both physi- and chemisorbed water.

The mass loss differences between air and nitrogen in the TGA (Figure S6a−c) and peak intensities around 300 °C in the DTA (Figure 5) are proportional to the amount of alumina in three different samples. From the FTIR data (Figure S5), we see hydrocarbon species from νC−H bands in alumina rich samples (CZ30A70, CZ50A50).

Thus, we presume that the mass differences between air and nitrogen in the TGA and peak intensities around 300 °C in the DTA are due to oxidation of organics trapped on the surfaces of the alumina rich samples.

At higher temperatures, we observe mass gains (TGA at ≥1200 °C) with a corresponding exotherm in the DTA (Figure 5). We believe this is attributable to the oxidation of $(Ce/Zr)^{3+}$ species substituting for Al^{3+} species in the δ-Al_2O_3 lattice during LF-FSP processing, as observed in previous studies.[24,25a] It seems reasonable to suggest that the $(Ce/Zr)^{3+}$ species in the δ-Al_2O_3 lattice segregate out during the δ to α-Al_2O_3 transformation and oxidize to $(Ce/Zr)O_2$ given the low solubility of these ions in α-Al_2O_3.[31]

In Table 2, we use these TGA mass gains to calculate approximate amounts of residual $(Ce/Zr)^{3+}$ species that oxidize during the δ- to α-Al_2O_3 transformation. Similar calculations were done for Zr^{3+} ions present in the δ-Al_2O_3 lattice in related work on $(ZrO_2)_x(Al_2O_3)_{1-x}$ core−shell nanopowders during transformation to α-Al_2O_3.[24] In these studies it was determined that the amounts of Zr^{3+} present are much higher than anticipated on the basis of the literature where its solubility in alumina was reported to be negligible.[24] These initial observations are now supported by the following XPS studies.

XPS Studies. XPS (see Experimental Section) was used to further quantify the amounts of Ce^{3+}/Zr^{3+} ions in our nanopowders. The XPS data for the CZ50A50 sample (Figure 6) indicate the presence of significant amounts of Ce^{3+} ions.[57−60] For comparative purposes the $(CeO_2)_x(Al_2O_3)_{1-x}$ data are provided in Figure 7. The XPS patterns for Ce^{3+}/Ce^{4+} in $(Ce_{0.7}Zr_{0.3}O_2)_x@(Al_2O_3)_{1-x}$ nanopowders are very similar to our previous $(CeO_2)_x(Al_2O_3)_{1-x}$ studies. The $Ce^{3+/4+}$ ratios obtained by quantification of the XPS data (CasaXPS program) are given in Table 3.

Because significant amounts of Ce^{3+} were observed in the $(CeO_x)_x(Al_2O_3)_{1-x}$ study with XPS patterns similar to the $(Ce_{0.7}Zr_{0.3}O_2)_x@(Al_2O_3)_{1-x}$ nanopowders, we assume that similar concentrations of Ce^{3+} are present in our $(Ce_{0.7}Zr_{0.3}O_2)_x@(Al_2O_3)_{1-x}$ nanopowders. These results are unexpected given that the LF-FSP process occurs in a highly oxidizing environment and may relate to core−shell effects wherein the shell prevents oxidation of the Ce^{3+} to Ce^{4+} in the highly oxidizing environment. Alternately, it suggests that some significant fraction of Ce^{3+} ions may be present in the δ-Al_2O_3 shell, which in retrospect is not surprising given our baseline studies.[24]

Consequently, we also sought to determine if there were significant alterations to the Zr^{3+} contents versus those expected based on the above calculations. Unfortunately, because of the relatively higher amounts and peak intensities of ceria in XPS, the intensities of the Zr ion peaks were negligible in the $(Ce_{0.7}Zr_{0.3}O_2)_x@(Al_2O_3)_{1-x}$ XPS data.[60−62]

As an alternative, we re-examined samples from our previously published work on $(ZrO_2)_{1-x}(Al_2O_3)_x$.[24a] The XPS studies for these materials are shown in Figure 8 along with NIST standards.[63]

The Figure 7a,b data coupled with the NIST XPS database and related studies on Zr ions[51−54] support the existence of mixtures of $Zr^{2+/3+/4+}$ ions in our $(ZrO_x)_x(Al_2O_3)_{1-x}$ materials. According to the NIST database and previous studies,[63−66] the XPS peak centered at 181.2 eV indicates the presence of zirconium suboxide containing significant amounts of $Zr^{2+/3+}$ ions. In the 13 and 50 mol % ZrO_x data in Figure 7, we observe mixtures of typical Zr^{4+} peaks (182 and 179.8 eV) and $Zr^{2+/3+}$ peaks (181.2 eV) as broad shapes.

The coexistence of Ce^{3+} and Zr^{3+} ions provides one possible explanation for the differences in the XRD data we report here and those of Sutorik and Baliat, or Stark, Madler, et al.[45,50] It may be that $(Ce^{3+}/Zr^{3+})_2O_3$ solid solutions form in LF-FSP processing that are more stable than previous expectations for these materials in oxidizing environments. A further point to be made is that the presence of $Zr^{2+/3+}$ species may be the reason these materials offer good catalytic activity for a variety of oxidizing reactions and the water gas shift reaction normally requiring Pt or Pd as a co-catalyst as found in the accompanying paper.[48] The development of Pt- or Pd-free catalysts for such

(57) Zhu, H. Y.; Hirata, T. *J. Mater. Sci. Lett.* **1993**, *12*, 749.
(58) Gigola, C. E.; Moreno, M. S.; Costilla, I. *Appl. Surf. Sci.* **2007**, *254*, 325.
(59) Brenier, R.; Mugnier, J.; Mirica, E. *Appl. Surf. Sci.* **1999**, *143*, 85.
(60) Galtayries, A.; Sporken, R.; Riga, J.; Blanchard, G.; Caudano, R. J. *Electron. Spectrosc. Relat. Phenom.* **1998**, *88−91*, 951.
(61) Wang, X.; Lu, G.; Guo, Y.; Xue, Y.; Jiang, L.; Guo, Y.; Zhang, Z. *Cat. Today* **2007**, *126*, 412.
(62) Nelson, A. E.; Schulz, K. H. *Appl. Surf. Sci.* **2003**, *210*, 206.
(63) NIST X-Ray Photoelectron Spectroscopy Database. (NIST Standard Reference Database 20, Version 3.5).
(64) Kumar, L.; Sarma, D. D.; Krummacher, S. *Appl. Surf. Sci.* **1988**, *32*, 309–319.
(65) Bastiannon, A.; Braicovich, L.; Michelis, B. D. *Surf. Sci.* **1992**, *264*, 423–428.
(66) De Gonzalez, C. O.; Garcia, E. A. *Surf. Sci.* **1988**, *193*, 305.

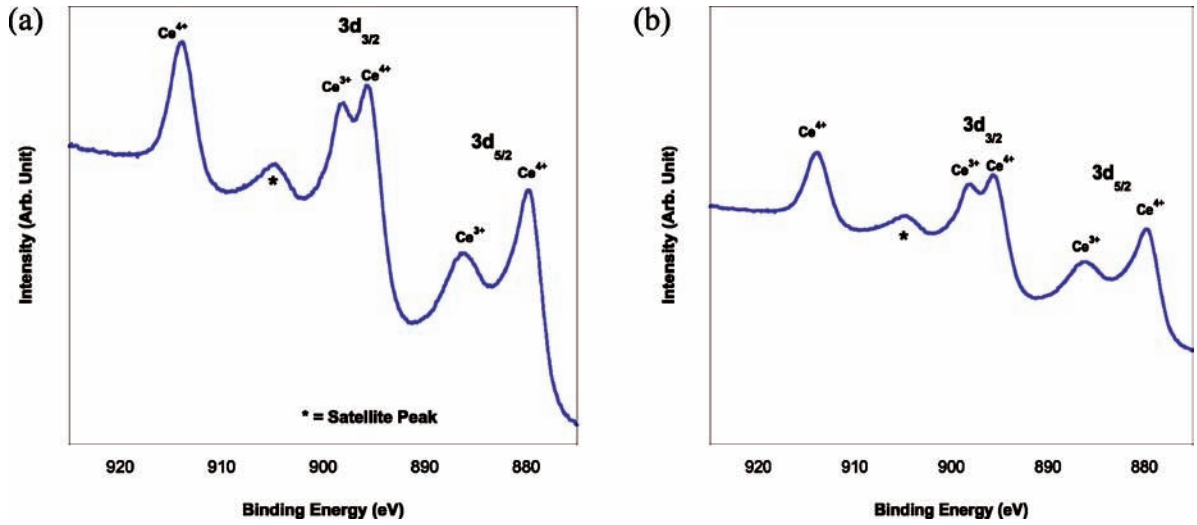

Figure 7. XPS of (a) 6 mol % CeO_x in Al_2O_3 (b) 75 mol % CeO_x in Al_2O_3.[24]

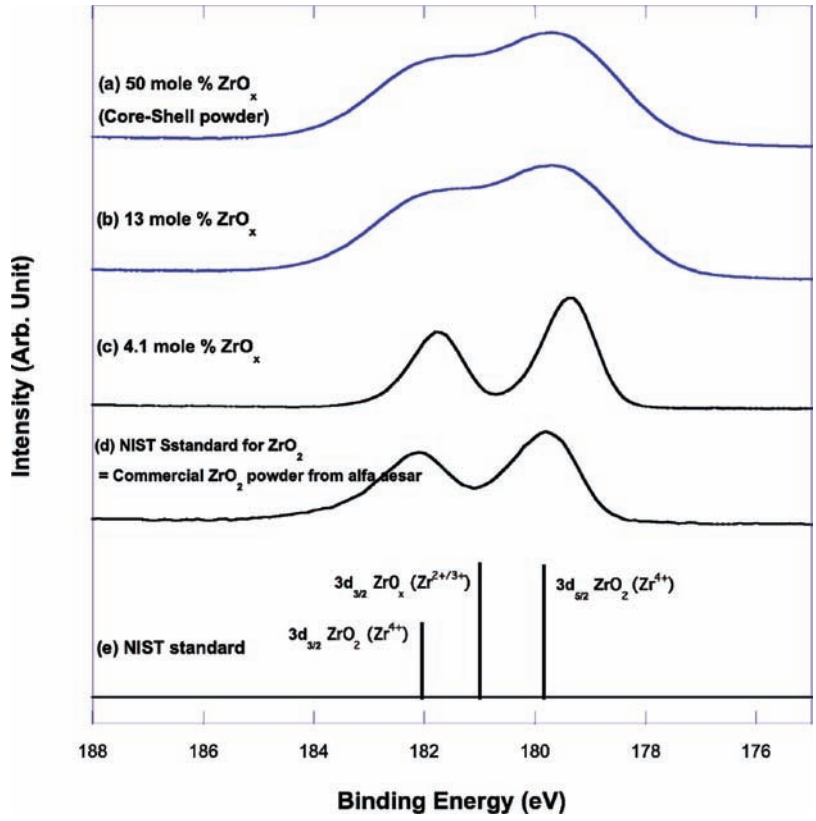

Figure 8. XPS analysis of $(ZrO_2)_{1-x}(Al_2O_3)_x$ ($x = 0-0.5$) nanopowders where (a) $x = 0.5$, (b) $x = 0.77$, and (c) $x = 0.96$.[24] (d) Equivalent to the NIST standard for ZrO_2. (e) NIST standard for ZrO_x.[63−66]

reactions would be of tremendous commercial importance and deserves further study.

As mentioned above, the single-crystal $Ce_{0.7}Zr_{0.3}O_2$ cores in these materials are spherical rather than faceted, as seen in Figure S4. This difference most likely arises because of the presence of Al^{3+} species during particle growth in the gas phase. Thus, a further argument for the distinct differences in catalytic behavior between our studies,[48] and the current literature on the behavior of these systems might result from the incorporation of Al^{3+} ions into the $Ce_{0.7}Zr_{0.3}O_2$ cores again changing their chemical reactivity.

Like many of our previous studies, LF-FSP as-produced nanopowders generated by rapid quenching provide access to novel kinetic products not expected from traditional processing methods that typically drive formation through thermodynamic control. Thus, these materials may offer unique opportunities for varieties of applications.

Conclusions

The above results suggest that LF-FSP processing can provide low-cost, efficient routes to well-known catalyst materials. The

accompanying paper[48] suggests that these materials offer novel properties not expected based on the performance of traditional catalysts.

LF-FSP provides access to $(CeO_x)_x(ZrO_2)_{1-x}$ and $(Ce_{0.7}Zr_{0.3}O_2)_{0.x}(Al_2O_3)_{1-x}$ mixed-metal oxide nanopowders with exceptional control of stoichiometry and phase purity. We were able to produce nanopowders of any composition in the Ce−Zr−O and Ce−Zr−Al−O systems with specific surface area of ≥ 30 m^2/g at rates of 50−100 g/h. We were able to produce nano $Ce_{0.7}Zr_{0.3}O_2$ solid solution single crystals in the $(CeO_x)_x(ZrO_2)_{1-x}$ and $(Ce_{0.7}Zr_{0.3}O_2)_{0.x}(Al_2O_3)_{1-x}$ systems.

Finally, we succeeded in producing core−shell nanoparticles in the $(Ce_{0.7}Zr_{0.3}O_2)_{0.x}(Al_2O_3)_{1-x}$ system in a single step with the correct choice of metalloorganic precursors. Because LF-FSP offers rapid quenching of the combustion species, it provides access to new, kinetic materials not accessible by any other conventional processing method. These nanopowders may offer novel potential for catalytic applications.

Acknowledgment. We would like to thank the Air Force Office of Scientific Research, through Contracts No. F49620-03-1-0389 and subcontract from UES Inc. F074-009-0041/AF07-T009, Maxit Inc., and Diamond Innovations Inc. for support of this work. We also thank Dr. George W. Graham (refs 40 and 46) for extensive discussions.

Supporting Information Available: Experimental analytical methods, including BET, XRD, SEM, TEM, DLS, FTIR, TGA-DTA, and XPS and selected corresponding data. This material is available free of charge via the Internet at http://pubs.acs.org.

JA9017545